Available online at www.sciencedirect.com
ScienceDirect
Acta Materialia 57 (2009) 4022–4031
Acta MATERIALIA
www.elsevier.com/locate/actamat

Evolution of nanoscale precipitates in Al microalloyed with Sc and Er

Richard A. Karnesky [a,1], David C. Dunand [a], David N. Seidman [a,b,*]

[a] Northwestern University, Department of Materials Science and Engineering, 2220 Campus Dr., Evanston. IL, 60208-3108, USA
[b] Northwestern University Center for Atom-Probe Tomography, 2220 Campus Dr., Evanston, IL 60208-3108, USA

Received 21 December 2008; received in revised form 14 April 2009; accepted 16 April 2009
Available online 6 June 2009

Abstract

The coarsening kinetics of nanoscale, coherent $Al_3(Sc_{1-x}Er_x)$ precipitates in α-Al during aging of a supersaturated Al–0.06 Sc–0.02 Er (at.%) alloy at 300 °C are studied using transmission electron microscopy and local-electrode atom-probe tomography. Erbium and Sc segregate at the precipitate core and shell, respectively. The matrix supersaturations of Er and Sc, as well as the mean precipitate radius and number density evolve in approximate agreement with coarsening models, allowing the determination of the matrix/precipitate interfacial free energy and solute diffusivities. At 300 °C, the $\alpha\text{-Al}/Al_3(Sc_{1-x}Er_x)$ interfacial free energy due to Sc is about twice as large as for $\alpha\text{-Al}/Al_3Sc$. The diffusivity of Er in the ternary alloy is about three orders of magnitude smaller than that of Er in binary Al–0.045 at.% Er and about two orders of magnitude smaller than the diffusivity of Sc in binary Al–Sc. The measured Sc diffusivity is consistent with the literature values.

Keywords: Aluminum alloys; Rare-earth elements; Scandium; Precipitation; Coarsening

1. Introduction

Al–Sc microalloys (below the maximum solubility of 0.23 at.% Sc) exhibit nanometric, coherent $Al_3Sc(L1_2)$ precipitates upon homogenizing, quenching, and aging. Together with a coarse grain size (mm-sized) achievable by casting, these precipitates impart good creep resistance to dilute Al–Sc binary alloys up to about 300 °C [1–12]. Much above this temperature, rapid coarsening of the precipitates leads to weakening of the alloy. Precipitates in dilute binary Al–Sc alloys coarsen in approximate agreement with the Lifshitz–Slyozov–Wagner (LSW) coarsening model [13,14] when aged at 300 °C and above. Experimentally-measured coarsening rates of the average precipitate radius differ [15,16], but several investigators found that the rates follow those predicted by that model [15,17–21]. Using transmission electron microscopy (TEM) and electrical-resistivity measurements, the temporal evolution of the mean precipitate radius and of the matrix supersaturation of Sc was determined for binary Al–Sc alloys between 400 and 500 °C, and was used to calculate the diffusivity of Sc in α-Al and the $\alpha\text{-Al}/Al_3Sc$ interfacial free energy [21]. Atom-probe tomography (APT) is particularly well suited for this kind of analysis because, unlike electrical-resistivity measurements, it provides direct, three-dimensional (3D) measurements of atomic concentration by counting atoms within a phase using no external standards or scaling assumptions.

Additional alloying elements in Al–Sc alloys can increase precipitate coarsening resistance, and thus raise the maximum service temperature from that of the binary alloys. For instance, Mg in solid solution in α-Al is found to decrease the coarsening rate of Al_3Sc precipitates [16,22]. Another example is Zr, which substitutes for Sc on the Sc sublattice of the $L1_2$ structure of the Al_3Sc precipitates.

* Corresponding author. Address: Northwestern University Center for Atom-Probe Tomography, 2220 Campus Dr., Evanston, IL 60208-3108, USA.
E-mail addresses: rakarne@sandia.gov (R.A. Karnesky), dunand@northwestern.edu (D.C. Dunand), d-seidman@northwestern.edu (D.N. Seidman).
URL: http://arc.nucapt.northwestern.edu/.
[1] Present address: Sandia National Laboratories, MS–9404, 7011 East Ave. Livermore, CA 94550, USA.

1359-6454/$36.00 © 2009 Acta Materialia Inc. Published by Elsevier Ltd. All rights reserved.
doi:10.1016/j.actamat.2009.04.034

These $Al_3(Sc_{1-x}Zr_x)$ precipitates exhibit significantly reduced coarsening kinetics compared to binary Al_3Sc precipitates due to the very small diffusivity of Zr in α-Al, which further segregates at the shell of the core–shell precipitates [20,23–28]. Hafnium and Ti also decrease the coarsening rate of Al_3Sc by the same mechanisms [7,29].

As compared to these transition metals, heavy rare-earth elements (RE)—including Er, Tm, Yb, and Lu—substitute in larger quantities within Al_3Sc precipitates [30], and can thus replace substantial quantities of the more expensive Sc. These RE also increase the lattice parameter mismatch between the $Al_3(Sc_{1-x}RE_x)$ precipitates and the α-Al matrix, thus enhancing the elastic interactions with dislocations and improving the creep resistance of the alloys [2,8]. We focus herein on Er because it is the least expensive of the heavy RE that forms stable $L1_2$ precipitates in α-Al [31,32] and Al_3Er has a larger lattice parameter (4.2 nm [33]) than the other Al_3RE intermetallics. Erbium is used in current aluminum alloys to refine grain sizes and thus improve strength at ambient temperature [34–43]. Erbium, however, diffuses faster than Sc in α-Al at 300 °C (the diffusivities are 4×10^{-19} m^2 s^{-1} [44] and 9×10^{-20} m^2 s^{-1} [45], respectively). Thus, Er may increase the coarsening kinetics of precipitates in ternary Al–Sc–Er alloys. Also, the low solid-solubility of Er in α-Al (0.046 at.% Er at 640 °C [44]) may reduce the maximum volume fraction of homogeneous precipitates, due to a reduction in solute concentration, as compared to binary Al–Sc alloys.

Herein, we present a study of an Al–0.06 Sc–0.02 Er (at.%) alloy and demonstrate that Er substitutes very substantially (up to at least 30%) for Sc in $Al_3(Sc_{1-x}Er_x)(L1_2)$ precipitates. We measure the kinetics of coarsening of these precipitates, from which we determine fundamental thermodynamic properties (interfacial free energies) and kinetic properties (diffusivities), which we compare to those of binary Al–Sc and Al–Er alloys.

2. Experimental methods

An Al–1 at.% Er master alloy was produced by non-consumable electrode arc-melting in argon from 99.9 at.% Er (Stanford Materials) and 99.99 at.% Al. The Al was found to contain no impurities in excess of 10 at. ppm, except for Fe, Cu, and Si (49, 42, and 40 at. ppm, respectively), which was measured by glow-discharge mass spectrometry (Shiva Technologies/Evans Analytical Group, Syracuse, NY). A ternary alloy, with nominal Al–0.06 Sc–0.02 Er (at.%) composition, was dilution cast from this master alloy employing the same stock of 99.99 at.% Al, and an Al–1.2 at.% Sc master alloy (KB Alloys). To increase the probability of the ternary alloy remaining in the single-phase α-Al field during homogenization, a temperature of 640 °C was selected, which is below the Al–Sc and Al–Er binary eutectic temperatures. The Sc and Er concentrations in the ternary alloy were chosen well below the maximum solubility limits in the respective binary Al–Sc and Al–Er alloys (0.23 at.% Sc [46] and ≈ 0.046 at.% Er [44]). The ternary alloy was melted in a zirconia-coated alumina crucible in a resistively-heated furnace at 750 °C in air. The melt was stirred to ensure proper mixing and then cast into a graphite mold resting on a copper plate to achieve relatively rapid rates of cooling and solidification. The chemical composition of the alloy was measured by ATI Wah Chang (Albany, OR) to be 0.064 ± 0.003 Sc and 0.022 ± 0.001 Er (at.%), corresponding to Al–0.11 Sc–0.14 Er (wt.%). The alloy was homogenized in air at 640 °C for 72 h and then quenched into ambient-temperature water. Aging was performed at 300 °C in air for between 24 and 1536 h (1–64 days) and was terminated by an ambient-temperature water quench. Local-electrode atom-probe (LEAP) tomography and TEM were performed on samples aged for 1, 4, 16, or 64 days. Additional LEAP tomography was performed on samples aged for 8 or 32 days.

Electron-transparent foils were prepared by mechanical grinding sections of aged specimens to a thickness of ≈ 100 μm. Discs of ≈3 mm diameter were then cut or punched. These discs were twin-jet electropolished in a Streuers TenuPol-5 at 20 Vdc using a 10 vol.% solution of perchloric acid in methanol chilled by a dry ice/methanol bath to −40 °C. TEM observations of precipitate size were performed with an Hitachi 8100 operating at 200 kV.

APT tips were prepared by cutting and grinding needles of the aged alloy to a cross-sectional area of $\approx 300 \times 300$ μm^2. These needles were electropolished in a 10 vol.% perchloric acid in acetic acid solution and then in a solution of 2 vol.% perchloric acid in butoxyethanol. A local-electrode atom-probe (LEAP) 3000X Si tomograph operating at a specimen temperature of 30 K in the voltage-pulsing mode (20% pulse fraction, as defined by the pulse voltage increment divided by the stationary voltage) was used to collect APT datasets. At least 5×10^7 atoms ranged inside windows of the mass-to-charge state (m/e) spectrum were collected for each aging treatment. 3D reconstructions were obtained using Imago's computer program IVAS. Because of the low concentration of Er in the alloy and because Er has six stable isotopes (not including Er hydrides that are also detected by LEAP tomography), background subtraction in the m/e spectra is critical to obtain accurate concentrations. Therefore, m/e windows twice as wide as the peak windows were made on either side of a peak (separated from the peak by at least half of the width of each peak's window). Because the total width of background windows is four times the peak width, the background-subtracted concentration is the number of ions in the peak with one fourth of the number of background events subtracted out, divided by the total ranged ions in a spectrum. The volume fraction of precipitates is calculated from the lattice parameters and fraction of atoms in the precipitate-phase. The far-field Sc and Er concentrations in α-Al were obtained employing proximity histograms (proxigrams) [47], which were calculated employing both the IVAS and APEX software programs [48].

3. Results

A uniform distribution of spheroidal $Al_3(Sc_{1-x}Er_x)$ precipitates is observed after aging the alloy at 300 °C for all aging times (24–1536 h), as shown in representative TEM micrographs in Fig. 1a and b and in an excerpt from a representative LEAP tomographic (3D) reconstruction in Fig. 2a. The precipitates are coherent, as demonstrated in Fig. 1a for a specimen aged for 1536 h, by the Ashby-Brown [49,50] strain-field contrast with lines of no contrast normal to the diffraction vector.

The 3D reconstructions of LEAP tomographic datasets containing 81 precipitates in samples aged for 96 h (Figs. 2 and 3) demonstrate that the precipitates have a core–shell structure. After 24 h aging, Er replaces 17 at.% of Sc in precipitates [41]. After 96 h aging, the amount of Sc replaced by Er increases to 30 at.%, where it remains approximately constant with aging for times as long as 1536 h (64 days). During this time, the Sc and Er interdiffuse and the precipitates grow and coarsen, decreasing the core/shell segregation effect. This near-stoichiometric trialuminide is expected from the very small solid-solubilities of both Sc and Er in α-Al [44,46] and the complete solubility between $Al_3Er(L1_2)$ and $Al_3Sc(L1_2)$ [33]. This confirms that Er can act as a partial substitute for Sc, therefore decreasing the cost of the alloy. Fig. 2b shows a single precipitate, with concentric 5 at.% isoconcentration surfaces for Sc and Er highlighting the Er-core/Sc-shell structure. Cylinders with orthogonal directions (determined by an indexed field-ion micrograph of the LEAP tip, as in Ref. [51]) used in 1D composition profiles, Fig. 3, indicate that segregation of the elements in the precipitate is greater along the [0 1 1]-direction than the [1 0 0]-direction, which is consistent with an anisotropy in interfacial free energy. Fig. 4 is a proxigram for samples aged 96 h, including the subvolume displayed in Fig. 2 (a total of 81 precipitates).

Fig. 5, shows that the precipitate volume fraction, ϕ, as measured by LEAP tomography, increases slightly from $\phi = 0.31 \pm 0.01\%$ after 24 h aging to $\phi = 0.33 \pm 0.02\%$ after 96 h aging. Between 96 h and 1536 h aging, ϕ remains essentially constant (within an experimental uncertainty of ≈0.02% per data point). It can thus be assumed that the system is in a quasi-stationary state. This constant value of measured precipitate volume fraction is the same as the equilibrium volume fraction, $\phi_{eq} = 0.33\%$ for an Al–0.08 at.% Sc binary alloy, as calculated using the lever rule [46] (due to the high solubility of Er in Al_3Sc and its low solubility in α-Al, discussed above).

The average precipitate radius, $\langle R \rangle$, increases with aging time at 300 °C, from 3.3 ± 0.2 nm after 24 h to 8 ± 2 nm after 1536 h aging, which is a factor of 2.4 ± 0.6 (Fig. 6). In the double-logarithmic plot, the data can be fit by a line with a slope of 0.24 ± 0.03. TEM was not performed on specimens aged for 192 h (8 days) or 768 h (32 days). In addition to the TEM results presented, $\langle R \rangle$ was determined from the spherical–equivalent radius for the number of atoms in whole precipitates. For earlier aging times, this analysis gave values of $\langle R \rangle$ consistent with the reported TEM measurements. For longer aging times, the LEAP tomographic data sets had only a few precipitates that were uncut by the boundary of the analysis volume and therefore $\langle R \rangle$ is not reported for them.

The $Al_3(Sc_{1-x}Er_x)$ precipitate number density, N_V, was found by counting individual precipitates isolated using the ENVELOPE method [52,53] and dividing by the volume of a LEAP tomographic data set (as obtained by using the total number of atoms in the data set, taking the 50% instrument efficiency into account). The number density of precipitates in Al–0.06 Sc–0.02 Er alloy decreases with aging time, Fig. 7. In this double-logarithmic plot, the data can be fit to a line with a slope of -0.9 ± 0.1.

The proxigram methodology was used to measure the far-field matrix concentrations of Sc and Er in the 3D LEAP reconstructions, taken at distances over 20 nm from the matrix/precipitate interface. These concentrations are plotted in Fig. 8 as a function of aging time raised to the power $-\frac{1}{3}$, the temporal exponent of the Kuehmann–Voorhees model for ternary alloys (described in detail in the

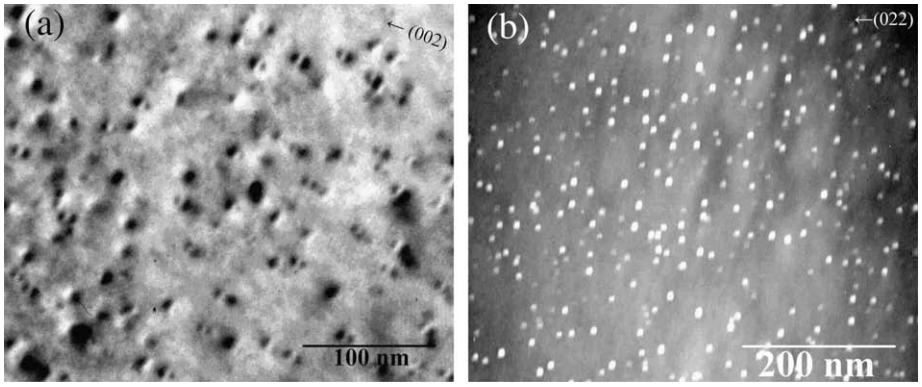

Fig. 1. Two-beam TEM micrographs of $Al_3(Sc_{1-x}Er_x)$ precipitates. In (a), the alloy aged at 300 °C for 1536 h (64 days) still has coherent precipitates, as observed by the Ashby-Brown strain-field contrast, imaged in bright field along the [1 0 0] zone axis using the $\bar{1}$ 1 1 reflection. In (b), a high number density ($(2.3 \pm 0.9) \times 10^{22}$ m^{-3}) of small ($\langle R \rangle = 3.7 \pm 0.9$ nm)$Al_3(Sc_{1-x}Er_x)$ precipitates is observed after aging for 96 h (4 days). Central-dark-field image using the 1 1 0 superlattice reflection on the [1 0 0] projection.

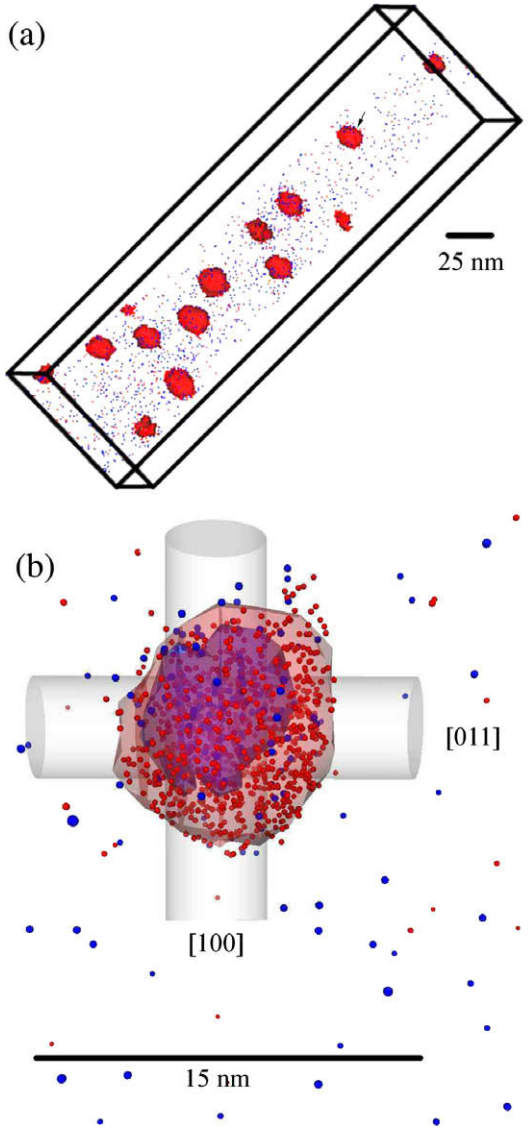

Fig. 2. A 3D reconstruction of a subvolume from a LEAP tomography dataset shows $Al_3(Sc_{1-x}Er_x)$ precipitates after aging for 96 h (4 days). The small red spheres represent Sc atoms and the larger blue spheres represent Er atoms (Al atoms are excluded for clarity). (a) Subvolume showing a high number density ($(2.3 \pm 0.9) \times 10^{22}$ m^{-3}) of precipitates. (b) Single precipitate with concentric 5 at.% isoconcentration surfaces for Sc and Er showing the Er-core/Sc-shell structure of many precipitates. Cylinders show the orthogonal directions [011] and [100], determined from an indexed field-ion microscopy image of the LEAP tip [51], used to calculate 1D concentration profiles. (For interpretation of the references to colour in this figure legend, the reader is referred to the web version of this article.)

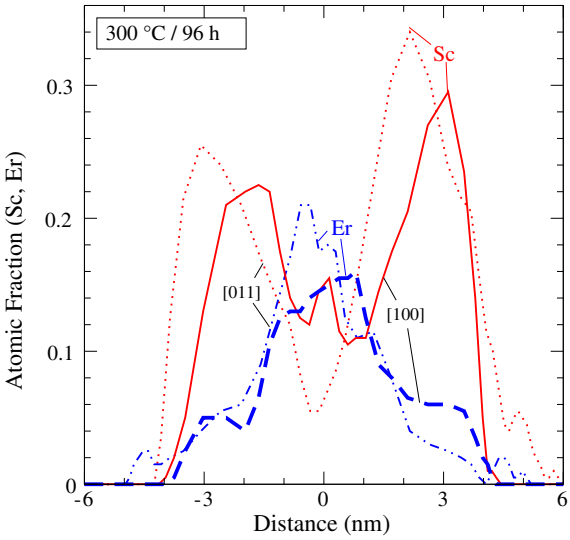

Fig. 3. Concentration profile along the orthogonal cylinders in Fig. 2b for two directions, [011] and [100] showing the core–shell structure of an $Al_3(Sc_{1-x}\ Er_x)$ precipitate.

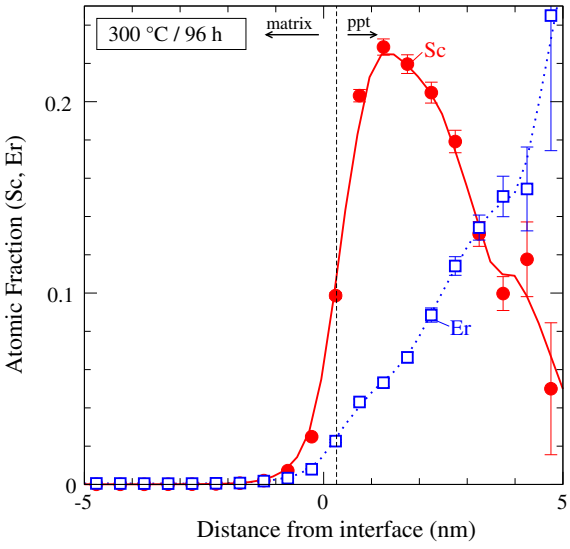

Fig. 4. Proxigram for samples aged 96 h, including the subvolume shown in Fig. 2 (a) (a total of 81 precipitates). Concentrations of Sc and Er are shown as a function of distance from the $\alpha - Al/Al_3(Sc_{1-x}Er_x)$ heterophase interface, which is defined by a 5 at.% Sc isoconcentration surface. Error bars are calculated using $\sigma_C = \sqrt{C(1-C)/N}$, where N is the total number of atoms detected.

next section). The far-field Sc concentration decreases with aging time from 40 ± 4 at. ppm after 24 h to 14 ± 2 at. ppm after 1536 h (64 days). This 65% decrease is greater than the average uncertainty of 30% (one standard deviation from counting statistics). Although there is much greater uncertainty in the Er concentration, it appears to decrease consistently with aging time by 60% from 10 ± 2 at. ppm to 4 ± 1 at. ppm over the same time period. This suggests that the estimated uncertainties are conservative numbers.

4. Discussion

4.1. Temporal evolution of precipitate radius

Umantsev and Olson showed analytically that the LSW model, which is valid only for dilute binary alloys with an equilibrium volume that is very small, could be extended to concentrated multicomponent alloys with the same time exponents but different rate constants [54]. Kuehmann and Voorhees (KV) analyzed the case of ternary alloys,

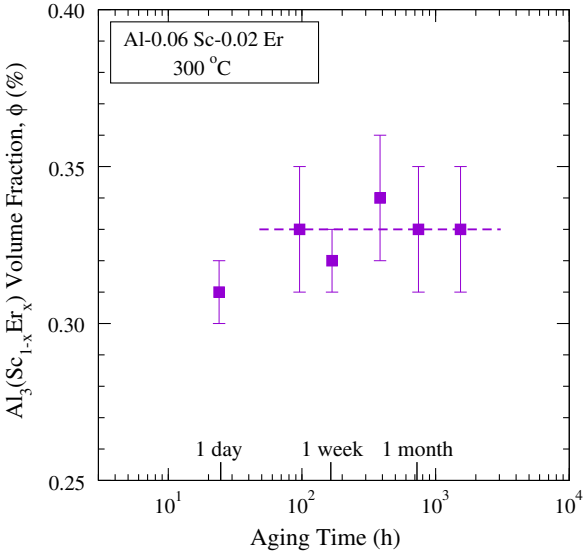

Fig. 5. Semi-logarithmic plot of $Al_3(Sc_{1-x}Er_x)$ volume fraction, ϕ, determined by LEAP tomography as a function of aging time at 300 °C. The horizontal dashed line with a slope of zero demonstrates that quasi-stationary state coarsening is achieved. Uncertainty has been propagated from the reported uncertainty in the lattice parameters of the two phases and from counting statistics of the number of atoms included in precipitates.

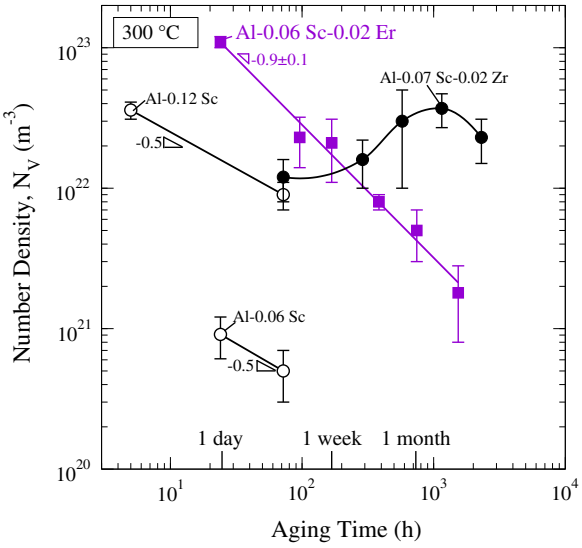

Fig. 7. Logarithmic plot of precipitate number density, N_V, versus aging time at 300 °C, as determined by LEAP tomography. The number density for Al–0.06 Sc–0.02 Er decreases steadily with a time exponent of -0.9 ± 0.1, found by fitting Eq. (2). The number density of precipitates in Al–Sc [15] and Al–Sc–Zr [25] alloys (both determined using TEM), with similar solute concentrations, exhibit smaller values of the slope over this time scale. Error bars are from counting statistics.

allowing for capillary effects [55]; these modifications are frequently ignored in the literature and only the classic LSW model for binary alloys is used. In the KV model, $\langle R(t)\rangle$ has a time dependence given by [55]:

$$\langle R(t)\rangle^n - \langle R(t_0)\rangle^n = K(t - t_0); \quad (1)$$

where K is a coarsening rate constant, t_0 is any time at or after the initiation of quasi-stationary state coarsening, and n is the inverse time exponent, which is predicted to be $n = 3$ (i.e., the time exponent is approximately $\frac{1}{n} = \frac{1}{3}$).

A non-linear least-squares fit to the four parameters in Eq. (1) was used to analyze the data shown in Fig. 6 to find

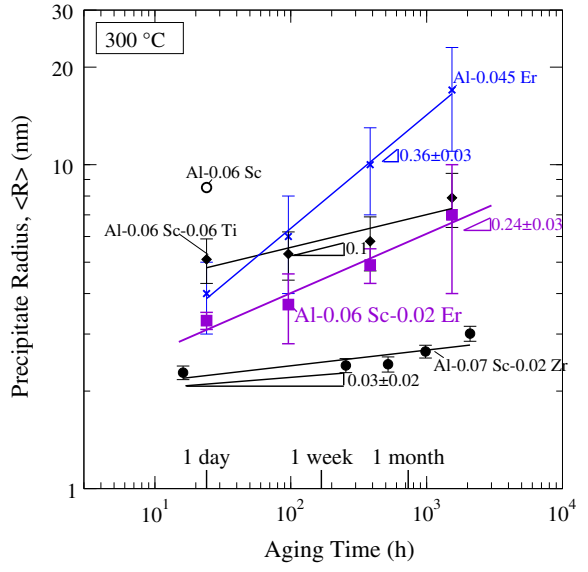

Fig. 6. Logarithmic plot of mean precipitate radius, $\langle R\rangle$ versus aging time at 300 °C, as determined by TEM. In Al–0.06 Sc–0.02 Er (at.%), $\langle R\rangle$ coarsens with a time exponent of 0.24 ± 0.03, found by a regression analysis of Eq. (1). This value is smaller compared to the value for Al–0.045 Er [44], but larger than for Al–0.06 Sc–0.06 Ti [7] and Al–0.07 Sc–0.02 Zr [25]. Error bars represent one standard deviation.

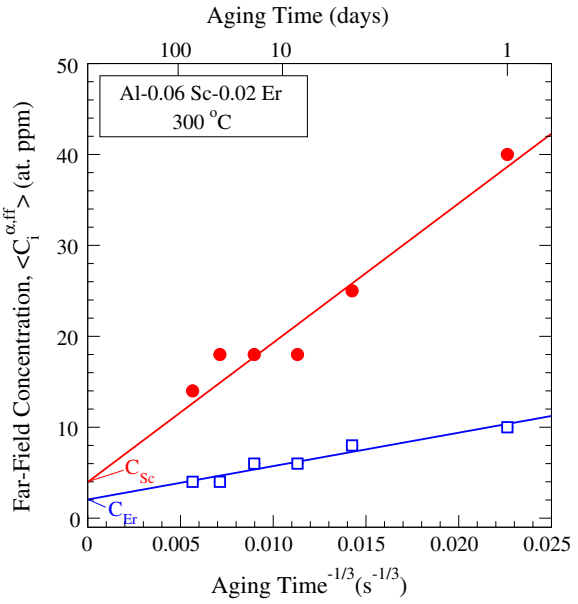

Fig. 8. Plot of the far-field concentration, $\langle C_i^{\alpha,ff}\rangle$, of Sc and Er in the α-Al matrix versus aging time raised to the $-\frac{1}{3}$ power at 300 °C. The concentration of Sc and Er determined by LEAP tomography steadily decrease with increasing aging time and the ordinate-intercept (infinite time) of the fitting line (Eq. (7)) gives the solid-solubility in α-Al at 300 °C.

values for $\langle R(t_0)\rangle$ and t_0. Because precipitate coarsening models are self-similar and scale-invariant, the only requirements are that $\langle R(t_0)\rangle$ is positive and that t_0 is at, or after, the onset of quasi-stationary state coarsening. The values found for these parameters fulfill these requirements, but do not have a fundamental meaning. Once $\langle R(t_0)\rangle$ and t_0 are found, they are used in a two parameter power-law fit of Eq. (1) to the data displayed in Fig. 6, yielding $\frac{1}{n} = 0.24 \pm 0.03$ and $K^R = (7 \pm 1) \times 10^{-31}$ m^3 s^{-1} (where the superscript R stands for radius).

The best-fit value for $\frac{1}{n}$ in Al–0.06 Sc–0.02 Er is smaller than both the predicted model value $\left(\frac{1}{n} = \frac{1}{3}\right)$ and the value found for an Al–0.045 at.% Er binary alloy $\left(\frac{1}{n} = 0.36 \pm 0.03\right)$ aged at 300 °C [44]. It is, however, greater than the exponent found for a binary Al–0.18 at.% Sc alloy aged at 300 °C $\left(\frac{1}{n} = 0.18 \pm 0.01\right)$ [15,16]. In a coarsening study of Al–2.2 Mg–0.12 Sc at 300 °C, a value $\frac{1}{n} = 0.16 \pm 0.02$ was found, and the disagreement with the theoretically-predicted value was attributed to either the dominance of a transient coarsening regime (with concurrent precipitate growth), or to the complexity of diffusion in ternary systems (off-diagonal terms of the diffusion tensor, nonzero value of the vacancy chemical potential, and diffusivity within the precipitate phase) [16]. It is probable that a transient coarsening regime is responsible for the small values of $\frac{1}{n}$ exhibited by the ternary alloys Al–0.06 Sc–0.06 Ti [7] and Al–0.07 Sc– 0.02 Zr [25] (illustrated in Fig. 6), given the very small diffusivities of Ti and Zr in α-Al compared to Sc and the segregation of these elements at the precipitate shell. For the present Al–0.06 Sc–0.02 Er alloy, the lack of perfect agreement with the theoretical value $\frac{1}{n} = \frac{1}{3}$ may also be due to the relatively narrow range of radii value considered (typically, an order of magnitude increase is preferred). In fact, quasi-stationary state coarsening can be assumed in view of the results obtained for $\phi(t)$ and the number density, $N_V(t)$ (Figs. 5 and 7). That the present Al–Sc–Er alloy achieves a time exponent closer to the model value than Al–Sc and Al–Sc–Mg is most likely due to the larger diffusivity of Er in α-Al as compared to Sc and the higher solubility of Er in the precipitates than Mg at 300 °C [44]; Mg is insoluble in Al_3Sc.

4.2. Temporal evolution of precipitate number density

As shown in Fig. 7, Zr additions increase the coarsening resistance of binary Al–Sc alloys very effectively, as the N_V value of $Al_3(Sc_{1-x}Zr_x)$ does not decrease significantly over many months [25]. Given the shallow slopes generated from the few data points reported for a binary Al–Sc in Fig. 7, the present Al–Sc–Er alloy seems to coarsen more rapidly than does Al–Sc. This is consistent with the diffusivity of Er being greater than that of Sc in α-Al at 300 °C [44].

The KV model for coarsening predicts that the precipitate number density, $\langle N_V(t)\rangle$ decreases with aging time according to [55]:

$$N_V(t)^m - N_V(t_0)^m \approx 4.74 \frac{K}{\phi_{eq}}(t - t_0). \tag{2}$$

A two-step regression analysis similar to that performed for $\langle R(t)\rangle$ was performed on $N_V(t)$ with the data of Fig. 7, yielding a time exponent of $\frac{1}{m} = -0.9 \pm 0.1$, which is approximately equal to the model value of $\frac{1}{m} = -1$. This good agreement indicates that the system may be near a stationary state, which is in agreement with the very small changes in ϕ with aging time (Fig. 5). Still, assuming the KV model can make correct predictions for this system, the fact that $\langle R(t)\rangle$ does not have an exact $\frac{1}{3}$ time dependence may imply that it is only in a quasi-stationary state. The minimum time to reach a stationary state can be estimated as the time for the 1D edge-to-edge inter-precipitate spacing ($\lambda^{1D}_{e-e}(t) \approx \left(\frac{1}{\phi(t)} - 1\right)\frac{4}{3}\frac{1.130}{1.046}\langle R(t)\rangle$ [56]) to equal the root–mean–square diffusion distance, $\sqrt{4Dt}$ [57]. Using the diffusion coefficient of the slower diffusing species (Sc), this time is calculated to be ≈200 h (≈8 days), indicating that the shortest annealing times (1 and 4 days) may not achieve an equilibrium state, as supported by the slightly smaller value of ϕ for samples aged for 1 day, Fig. 5.

A rate constant of $K^{N_V} = (7 \pm 1) \times 10^{-32}$ m^3 s^{-1} was obtained from the fitting procedure of Eq. (2) and the $N_V(t)$ data in Fig. 7, as the superscript N_V to K denotes. This differs by one order of magnitude from the value $K^R = (7 \pm 1) \times 10^{-31}$ m^3 s^{-1} found above using Eq. (1) and $\langle R(t)\rangle$ data in Fig. 6. This may be because the mean-field KV model does not describe this core–shell system, but it is worth noting that the regression of Eq. (1) had fewer data points and a smaller span than the regression of Eq. (2).

4.3. The rate constant, K

The KV model value for the coarsening constant, K_{KV}, is calculated assuming dilute ideal-solution theory [55]:

$$K_{KV} = \frac{8\gamma^{\alpha/\beta}V_m^{\beta}}{9\Lambda}; \tag{3}$$

where $\gamma^{\alpha/\beta}$ is the isotropic interfacial free energy, V_m^{β} is the molar volume of $Al_3(Sc_{1-x}Er_x)$ ($V_m^{\beta} = \frac{N_a a^3}{4} = 1.06 \times 10^{-5}$ m^3 mol^{-1}, where N_a is Avogadro's number and a is the lattice parameter of $Al_3(Sc_{1-x}Er_x)$, found from those of Al_3Sc and Al_3Er assuming Vegard's law [33,58]), and the parameter Λ is given by:

$$\Lambda = \frac{\Delta C_{Sc}}{D_{Sc}}\left(\Delta C_{Sc}G^{\alpha}_{Sc,Sc} + \Delta C_{Er}G^{\alpha}_{Sc,Er}\right) + \frac{\Delta C_{Er}}{D_{Er}}\left(\Delta C_{Er}G^{\alpha}_{Er,Er} + \Delta C_{Sc}G^{\alpha}_{Sc,Er}\right); \tag{4}$$

where the value $\Delta C_i = C_i^{\beta} - C_i^{\alpha}$ is the difference in the equilibrium solid-solubility of component i between the $Al_3(Sc_{1-x}Er_x)$ precipitate-phase, β, and the α-Al matrix-phase. $C^{\alpha,eq}_{Sc} = 7.2 \times 10^{-6}$ (expressed as an atomic fraction) [16] and $C^{\alpha,eq}_{Er} = 4 \times 10^{-6}$ [44]. For C_i^{β}, it is assumed that the precipitate-phase is a trialuminide with the Er/Sc ratio of

the overall alloy composition (as Er is fully soluble in Al_3Sc). The quantity D_i is the diffusivity of the solute species i in α-Al ($D_{Sc} = 9.01 \times 10^{-20}$ m^2 s^{-1} [45] and $D_{Er} = 4 \times 10^{-19}$ m^2 s^{-1} [44] at 300 °C) and $G^{\alpha}_{i,j}$ is the partial derivative of the molar Gibbs free energy of the α-phase with respect to components i and j. For an ideal dilute solid solution, they are given by:

$$G^{\alpha}_{i,i} = \frac{R_g T(1 - C^{\alpha,eq}_j)}{C^{\alpha,eq}_i\left(1 - C^{\alpha,eq}_i - C^{\alpha,eq}_j\right)}, \quad (5)$$

$$G^{\alpha}_{i,j} = \frac{R_g T}{1 - C^{\alpha,eq}_i - C^{\alpha,eq}_j}; \quad (6)$$

where R_g is the ideal gas constant. The interfacial free energy for the $Al_3(Sc_{1-x}Er_x)$/α-Al interface is unknown. Because the shell of the precipitates is very rich in Sc, the value $\gamma^{\alpha/\beta}_{Sc} = 0.5 \pm 0.2$ J m^{-2} determined experimentally, as described in the following paragraph, was used. With $\gamma^{\alpha/\beta}_{Sc}$ and the other parameters entering Eqs. (4)–(6), the theoretical value for K_{KV} is calculated from Eq. (3) to be $(1.7 \pm 0.7) \times 10^{-32}$ m^3 s^{-1}. Table 1 summarizes the results of how the coarsening constant K was calculated in three ways: (i) as K^R, from a fit to the experimental measurements of the temporal evolution of $\langle R \rangle$ to Eq. (1); (ii) as K^{N_V}, from a fit of experimental measurements of the temporal evolution of N_V to Eq. (2); and (iii) as K_{KV}, from Eq. (3). There is better agreement between K_{KV} and K^{N_V} than between K_{KV} and K^R. This is consistent with the better agreement to the model value of temporal exponent for $N_V(t)$ than for $\langle R(t) \rangle$ and may indicate that the $N_V(t)$ data yields more credible physical constants from the KV model than does $\langle R(t) \rangle$, possibly due to the greater number of data points and the more significant span in N_V.

4.4. Temporal evolution of matrix concentration

In the KV coarsening model, the matrix supersaturation, $\Delta C^{\alpha}_i(t)$, evolves as [55]:

$$\Delta C^{\alpha}_i(t) = \langle C^{\alpha,ff}_i(t) \rangle - C^{\alpha,eq}_i(\infty) = \kappa^{\alpha}_{i,KV}(t)^q; \quad (7)$$

where $\langle C^{\alpha,ff}_i \rangle$ is the far-field concentration for component i, $C^{\alpha,eq}_i$ is the equilibrium solubility of i in the α-Al matrix, $\kappa^{\alpha}_{i,KV}$ is a rate constant (which is different from the coarsening constant K), and the temporal exponent $q = -\frac{1}{3}$.

Table 1
The rate constant, K(m^3 s^{-1}), with standard fitting errors.

Measured from $N_V(t)$, K^{N_V}	$(7 \pm 1) \times 10^{-32}$
Measured from $\langle R(t) \rangle$, K^R	$(7 \pm 1) \times 10^{-31}$
$\frac{K^{N_V}}{K^R}$	0.10 ± 0.02
Calculated from Eq. (3), K_{KV}	$(1.7 \pm 0.7) \times 10^{-32}$
$\frac{K^{N_V}}{K_{KV}}$	4 ± 2
Measured for Al–0.18 Sc binary, K^{Sc} [15]	$(2.0 \pm 0.4) \times 10^{-32}$
$\frac{K^{N_V}}{K^{Sc}}$	3.5 ± 0.9
Measured for Al–0.045 Er binary, K^{Er} [44]	$(2 \pm 1) \times 10^{-31}$
$\frac{K^{N_V}}{K^{Er}}$	0.4 ± 0.2

A linear regression analysis was performed on the data displayed in Fig. 8, where the far-field concentrations, $\langle C^{\alpha,ff}_i \rangle$, of Sc and Er in the α-Al matrix are plotted as a function of aging time at 300 °C raised to the $-\frac{1}{3}$ power. Extrapolations to infinite time $\left(t^{-\frac{1}{3}} = 0\right)$ yield the equilibrium solid-solubilities of Sc and Er in α-*Al* at 300 °C, according to Eq. (7). For Sc, $C^{\alpha,eq}_{Sc}$ is 4 ± 2 at. ppm Sc, which is less than, but most likely within experimental error of the calculated value of 7 at. ppm Sc for the Al–Sc binary system [16]. For Er, the extrapolation to infinite time yields $C^{\alpha,eq}_{Er} = 2 \pm 1$ at. ppm Er, which is equal, within error, to the value of 4 ± 3 at. ppm Er measured in the Al–0.045 Er binary system [44].

The power-law regression to Eq. (7) yields $q = -0.35 \pm 0.03$ for Sc and $q = -0.32 \pm 0.04$ for Er, in good agreement with the KV value of $-\frac{1}{3}$. The rate constants are found to be $\kappa^{\alpha}_{Sc} = (1.8 \pm 0.8) \times 10^{-3}$ at. fr. $s^{\frac{1}{3}}$ and $(\kappa^{\alpha}_{Er} = 3 \pm 2) \times 10^{-3}$ at. fr. $s^{\frac{1}{3}}$. These can be compared to the theoretical KV expression for κ^{α}_i, which is [55]:

$$\kappa^{\alpha}_{i,KV} = \frac{\left(3\gamma^{\alpha/\beta}V^{\beta}_m\right)^{\frac{2}{3}}A^{\frac{1}{3}}\Delta C_i}{\Delta C_i\left(\Delta C_i G^{\alpha}_{i,i} + \Delta C_j G^{\alpha}_{i,j}\right) + \Delta C_j\left(\Delta C_j G^{\alpha}_{j,j} + \Delta C_i G^{\alpha}_{i,j}\right)}; \quad (8)$$

where $\gamma^{\alpha/\beta}_i$ is the interfacial free energy between the α-Al matrix and the $Al_3(Sc_{1-x}Er_x)$ precipitates. The KV model does not account for core/shell precipitates, and $\gamma^{\alpha/\beta}_i$ only considers a single solute species (i). Using the value for Sc, because this element partitions to the precipitate shell, $\gamma^{\alpha/\beta}_{Sc} = 0.5 \pm 0.2$ J m^{-2} (calculated in the following section), Eq. (8) yields $\kappa^{\alpha}_{Sc,KV} = (2.3 \pm 0.8) \times 10^{-3}$ at. fr. $s^{\frac{1}{3}}$ and $\kappa^{\alpha}_{Er,KV} = (9 \pm 3) \times 10^{-4}$ at. fr. $s^{\frac{1}{3}}$. These are in excellent

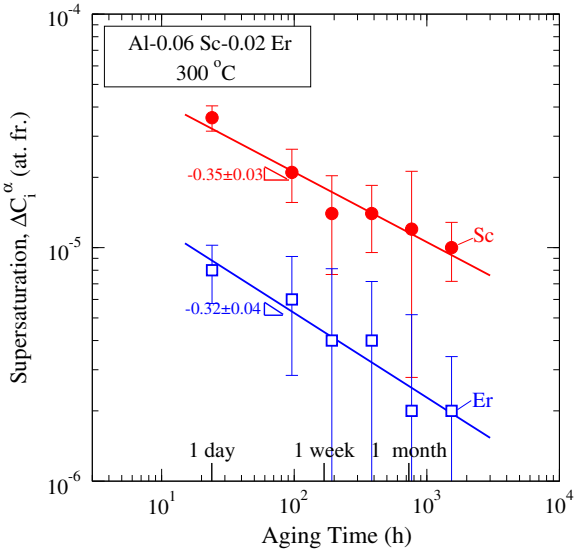

Fig. 9. Logarithmic plot of supersaturation of Sc and Er, ΔC^{α}_i, in the α-Al matrix versus aging time at 300 °C. The solid-solubility of Er in α-Al is determined from Fig. 8 and a second refinement was made to fit the coarsening prefactor and time exponent. Uncertainty has been propagated from the individual concentration measurements and the fitting error in the solid-solubility.

Table 2
The rate constant, κ (at. fr. $s^{\frac{1}{3}}$), with standard fitting errors.

Measured κ^{α}_{Sc}	$(1.8 \pm 0.8) \times 10^{-3}$
Calculated $\kappa^{\alpha}_{Sc,KV}$ from Eq. (8)	$(2.3 \pm 0.8) \times 10^{-3}$
Measured κ^{α}_{Er}	$(3 \pm 2) \times 10^{-3}$
Calculated $\kappa^{\alpha}_{Er,KV}$ from Eq. (8)	$(9 \pm 3) \times 10^{-4}$

agreement with the experimentally determined values from the best-fits of data in Fig. 9, reported above ($\kappa^{\alpha}_{Sc} = (1.8 \pm 0.8) \times 10^{-3}$ at. fr. $s^{\frac{1}{3}}$ and $\kappa^{\alpha}_{Er} = (3 \pm 2) \times 10^{-3}$ at. fr. $s^{\frac{1}{3}}$). Values of κ^{α}_{i} are listed in Table 2.

4.5. Precipitate/matrix interfacial free energy

Following Ref. [16], the interfacial free energy between two phases (α and β), $\gamma^{\alpha/\beta}_{i}$, is found from Eqs. (3)–(8) as:

$$\gamma^{\alpha/\beta}_{i} = \frac{\kappa^{\alpha}_{i,KV} K^{\frac{1}{3}}_{KV} \left(\Delta C_i \left(\Delta C_i G^{\alpha}_{i,i} + \Delta C_j G^{\alpha}_{i,j}\right) + \Delta C_j \left(\Delta C_j G^{\alpha}_{j,j} + \Delta C_i G^{\alpha}_{i,j}\right)\right)}{2 V^{\beta}_{m} \Delta C_i}. \quad (9)$$

Using the experimentally determined values of $K^{N_V} = (7 \pm 1) \times 10^{-32}$ m^3 s^{-1}, $\kappa^{\alpha}_{Sc} = (1.8 \pm 0.8) \times 10^{-3}$ at. fr. $s^{\frac{1}{3}}$, and $\kappa^{\alpha}_{Er} = (3 \pm 2) \times 10^{-3}$ at. fr. $s^{\frac{1}{3}}$, it is found from Eq. (9) that $\gamma^{\alpha/\beta}_{Sc} = 0.5 \pm 0.2$ J m^{-2} and $\gamma^{\alpha/\beta}_{Er} = 3 \pm 2$ J m^{-2} (where the uncertainty is propagated from the uncertainties in K^{N_V} and κ^{α}_{i} only). The mean value found for $\gamma^{\alpha/\beta}_{Sc}$ is larger than values found for other Al–Sc alloys, but is still comparable when the uncertainty is considered. In the Al–Sc binary system, $\gamma^{\alpha/\beta}_{Sc}$ has been found to be between 0.02 and 0.3 J m^{-2} [18,19,21,59–63], with values of ≈ 0.2 J m^{-2} being a reasonable average for the {100}-, {110}-, and {111}-facets; experimental measurements near this value have relied on extrapolation of the high-temperature diffusivity and first-principles calculations in this range have used more accurate values for the formation energy of Al_3Sc [61]. Using a similar methodology as is employed in the present paper, $\gamma^{\alpha/\beta}_{Sc}$ for two Al–Mg–Sc alloys with different compositions (Al–2.2 Mg–0.12 Sc and Al–1 Mg–0.16 Sc) was determined to be between 150 and 225 mJ m^{-2} [16,22], with more solute segregation measured at the {110}- and {111}-facets, which have larger interfacial free energies than the {100}-facet [64]. The larger values of $\gamma^{\alpha/\beta}_{Sc}$ in these ternary systems are consistent with the smaller values of the solid-solubility of Sc in α-Al that is found in these studies as compared to Al–Sc binary alloys and with an increase in the interfacial free energy due to Er, which is most likely an electronic (chemical) effect. The interfacial free energy of Al–Sc–Er is also anisotropic [65], Fig. 3.

The value found for $\gamma^{\alpha/\beta}_{Er}$ is unusually large (the surface energy of pure Al is ≈ 1 J m^{-2} [66,67]), although there is a significant uncertainty due to the large uncertainty in κ^{α}_{Er}, which is, itself, due to the small concentration of Er. This large value suggests perhaps that the assumptions of Eq. (9) are not fulfilled by this alloy. In particular, the segregation of Er to the core of the $Al_3(Sc_{1-x}Er_x)$ precipitates might change the dependence of K and κ on $\gamma^{\alpha/\beta}_{Er}$ (Eqs. (3) and (8)). The KV model neglects the off-diagonal terms in the diffusivity matrix (Onsager coefficients [68]) and, while we assume that dilute ideal-solution theory applies, there are most likely solute–vacancy and solute–solute interactions in this system that are important. The Sc segregation at the precipitate shell may help explain why the experimentally determined values of $\gamma^{\alpha/\beta}_{Sc}$ and (as shown in the subsequent section) D_{Sc} are in more reasonable agreement with prior studies of Al–Sc alloys.

The result that $\gamma^{\alpha/\beta}_{Er} > \gamma^{\alpha/\beta}_{Sc}$ is, however, consistent with Sc segregating at the shell and Er segregating at the core of the precipitates. It is also consistent [65] with the unconstrained lattice parameter misfit between the α-Al matrix and Al_3Er being larger than between α-Al and Al_3Sc (3.0% [33] versus 1.4% [69]).

4.6. Sc and Er diffusivities in α–Al

Unlike previous work on Al–Mg–Sc alloys, where the diffusivities of Sc and Mg are very disparate (allowing the use of simplified equations [16]), the diffusivities and solid-solubilities of Er and Sc in α-Al in binary alloys at 300 °C are similar [44]. Therefore terms that are neglected in Ref. [16] must be included. This leads to our derivation of a more complicated equation for the diffusivity of the species i, D_i, given by:

$$D_i = \frac{9\left(\Delta C_i G^{\alpha}_{i,i} + \Delta C_j G^{\alpha}_{i,j}\right) \Delta C_i^3 K^{\frac{2}{3}}_{KV}}{4\kappa^{\alpha}_{i,KV}\eta - 9\frac{\Delta C_j}{D_j}\left(\Delta C_j G^{\alpha}_{j,j} + \Delta C_i G^{\alpha}_{i,j}\right)\Delta C_i^2 K^{\frac{2}{3}}_{KV}}; \quad (10)$$

where:

$$\eta = \Delta C_i \left(\Delta C_i G^{\alpha}_{i,i} + \Delta C_j G^{\alpha}_{i,j}\right) + \Delta C_j \left(\Delta C_j G^{\alpha}_{j,j} + \Delta C_i G^{\alpha}_{i,j}\right). \quad (11)$$

The equation that led to this solution of D_i and a review of the past approximation is given in Appendix A. Introducing the measured values into Eq. (10) yields $D_{Sc} = (6 \pm 3) \times 10^{-20}$ m^2 s^{-1}, which is within experimental error of the diffusivity of Sc in pure Al at 300 °C found from radioactive tracer measurements (9.01×10^{-20} m^2 s^{-1} [45]). Erbium has a negligible effect on the mobility of Sc. The calculated value of $D_{Er} = (9 \pm 6) \times 10^{-22}$ m^2 s^{-1} in the present ternary alloy is, however, three orders of magnitude smaller than in a binary Al–0.045 Er alloy ($D_{Er} = (4 \pm 2) \times 10^{-19}$ m^2 s^{-1} [44]). A similar reduction is observed in the diffusivity of Yb in Al–0.06 Sc–0.02 Yb compared to Al–0.03 Yb ($(5 \pm 4) \times 10^{-21}$ m^2 s^{-1} and $(6 \pm 2) \times 10^{-17}$ m^2 s^{-1}, respectively [70]). These reductions are consistent with the greater coarsening resistance of the ternary Al–0.06 Sc–0.02 RE alloys as compared to the Al–RE binary alloys containing either Er or Yb, and may arise from the core–shell structure of $Al_3(Sc_{1-x}RE_x)$ precipitates and/or to vacancy–solute and solute–solute interactions that are not considered in dilute ideal-solution theories. The KV analysis neglects the off-diagonal terms of the Onsager diffusivity matrix, which impacts coarsening [71]. Similar coarsening

phenomena have been observed in dilute Al–Sc–Zr [23–28,72,73] and Al–Sc–Ti [7] alloys, where the slower moving Zr or Ti atoms partition at shells around $Al_3(Sc_{1-x}M_x)$ precipitates and retard coarsening as compared to binary Al–Sc alloys.

5. Conclusions

Upon aging at 300 °C, the supersaturated ternary Al–0.06 Sc–0.02 Er (at.%) alloy forms nanoscale $Al_3(Sc_{1-x}Er_x)$ precipitates whose evolution was followed by 3D local-electrode atom-probe tomography and transmission electron microscopy, leading to the following conclusions:

- For aging times between 1 and 64 days, coherent ($L1_2$), near-stoichiometric $Al_3(Sc_{1-x}Er_x)$ precipitates are formed with a *core–shell* structure, with Sc and Er segregated at the shells and cores, respectively.
- The amount of Sc replaced by *Er in precipitates* increases with aging time from 17 at.% after 24 h to 30% after 96 h, and is nearly constant for prolonged aging times. This demonstrates that Er can efficiently replace the more expensive Sc within the precipitates.
- The *number density* of $Al_3(Sc_{1-x}Er_x)$ precipitates is initially greater than in Al–0.06 Sc and Al–0.045 Er binary alloys. It decreases with a time exponent of $m = -0.9 \pm 0.1$, in approximate agreement with the Kuehmann–Voorhees (KV) model value of -1 and more quickly than in Al–0.06 Sc.
- The time exponent for the mean *radius* of $Al_3(Sc_{1-x}Er_x)$ precipitates $\left(\frac{1}{n} = 0.24 \pm 0.03\right)$ is smaller than the value of $\frac{1}{3}$ predicted by the KV model and intermediate between values measured for Al–0.045 at.% Er $\left(\frac{1}{n} = 0.36 \pm 0.03\right)$ and Al–0.18 Sc $\left(\frac{1}{n} = 0.18 \pm 0.01\right)$ alloy aged at 300 °C.
- The time exponents for the *matrix supersaturation* are -0.35 ± 0.03 for Sc and -0.32 ± 0.04 for Er, both in agreement with the KV model value of $-\frac{1}{3}$.
- From the above coarsening measurements, the *interfacial free energy* between the $Al_3(Sc_{1-x}Er_x)$ precipitates and α-Al matrix is 0.5 ± 0.2 J m^{-2}, which is larger than has been measured in other Al–Sc alloys, possibly due to the electronic (chemical) effect of Er in this alloy.
- From the above coarsening measurements, the *diffusivity* of Sc is calculated as $D_{Sc} = (6 \pm 3) \times 10^{-20}$ m^2 s^{-1}, which is in good agreement with radioactive tracer experiments of Sc in pure Al (9.01×10^{-20} m^2 s^{-1} [45]). The calculated value of $D_{Er} = (9 \pm 6) \times 10^{-22}$ m^2 s^{-1} in the ternary alloy is three orders of magnitude smaller than the value determined in an Al–0.045 Er binary alloy ($D_{Er} = (4 \pm 2) \times 10^{-19}$ m^2 s^{-1} [44]) at 300 °C, indicating that the KV model and the diffusivity in the binary alloy do not describe this ternary system well. This may be due to the core–shell structure of precipitates or to solute–solute and solute–vacancy interactions that have been omitted.

Acknowledgements

This research is supported by the US Department of Energy through grant DE–FG02–98ER45721. Atom-probe tomographic measurements were performed at the Northwestern University Center for Atom-Probe Tomography (NUCAPT), using a LEAP tomograph purchased with funding from the NSF-MRI (DMR–0420532, Dr. Charles Bouldin, monitor) and ONR-DURIP (N00014–0400798, Dr. Julie Christodoulou, monitor) programs. Dr. Dieter Isheim is thanked for managing NUCAPT. The authors thank Drs. Z. Mao and M. van Dalen, and Mr. C. Booth-Morrison (all of Northwestern University) for useful conversations.

Appendix A. Previous approximations of Eq. (10)

In Ref. [16], it was shown that:

$$\frac{4}{9}\frac{\kappa_{KV}}{\Delta C_i}\frac{\Delta C_i\left(G^{\alpha}_{i,i}+\Delta C_j G^{\alpha}_{i,j}\right)+\Delta C_j\left(\Delta C_i G^{\alpha}_{i,j}+\Delta C_j G^{\alpha}_{j,j}\right)}{K_{KV}^{\frac{2}{3}}\Delta C_i} = \frac{\Delta C_i}{D_i}\left(\Delta C_i G^{\alpha}_{i,i}+\Delta C_j G^{\alpha}_{i,j}\right)+\frac{\Delta C_j}{D_j}\left(\Delta C_i G^{\alpha}_{i,j}+\Delta C_j G^{\alpha}_{j,j}\right). \tag{12}$$

Solving for D_i yields Eq. (10). Because $D_{Mg} \gg D_{Sc}$, Ref. [16] makes the approximation $D_{Mg} \to \infty$, reducing Eq. (10) to:

$$D_{Sc} = \frac{9\left(\Delta C_{Sc} G^{\alpha}_{Sc,Sc} + \Delta C_{Mg} G^{\alpha}_{Sc,Mg}\right)\Delta C_{Sc}^3 K_{KV}^{\frac{2}{3}}}{4\kappa^{\alpha}_{Sc,KV}\left(\Delta C_{Sc}\left(\Delta C_{Sc} G^{\alpha}_{Sc,Sc} + \Delta C_{Mg} G^{\alpha}_{Sc,Mg}\right) + \Delta C_{Mg}\left(\Delta C_{Mg} G^{\alpha}_{Mg,Mg} + \Delta C_{Sc} G^{\alpha}_{Sc,Mg}\right)\right)}. \tag{13}$$

Note that Eq. (12) in Ref. [16] is incorrect—either a ΔC_{Sc} term should not have been canceled and the terms following $4\kappa_{KV}$ in the denominator should be enclosed in parentheses or the ΔC_{Mg} term should be dropped completely. This typographical error does not affect the result because $\Delta C_{Sc} \gg \Delta C_{Mg}$ and substituting the values of Ref. [16] into either the equation given in the reference, or this paper's Eq. (10), or Eq. (13) yields the same value, $D_{Sc} = 1.3 \times 10^{-20}$ m^2 s^{-1}.

References

[1] Fuller CB, Seidman DN, Dunand DC. Scripta Mater 1999;40:691–6.
[2] Marquis EA, Dunand DC. Scripta Mater 2002;47:503–8.
[3] Fuller CB, Seidman DN, Dunand DC. Acta Mater 2003;51:4803–14.
[4] Marquis EA, Seidman DN, Dunand DC. Acta Mater 2003;53:4751–60.
[5] Deshmukh SP, Mishra RS, Kendig KL. Mater Sci Eng A 2004;381:381–5.
[6] Deshmukh SP, Mishra RS, Kendig KL. Mater Sci Eng A 2005;410–411:5 3–57.
[7] van Dalen ME, Dunand DC, Seidman DN. Acta Mater 2005;53:4225–35.
[8] Karnesky RA, Seidman DN, Dunand DC. Mater Sci Forum 2006;519–521:1035–40.
[9] van Dalen ME, Dunand DC, Seidman DN. J Mater Sci 2006;41:7814–23.

[10] van Dalen ME, Gyger T, Dunand DC, Seidman DN. Microsc Microanal 2007;13:1618–9.
[11] van Dalen ME, Seidman DN, Dunand DC. Acta Mater 2008;56:4369–77.
[12] Røyset J, Ryum N. Int Mater Rev 2005;50:19–44.
[13] Lifshitz IM, Slyozov VV. J Phys Chem Solids 1961;19:35–50.
[14] Wagner C. Z Elektrochem 1961;65:581–91.
[15] Marquis EA, Seidman DN. Acta Mater 2001;49:1909–19.
[16] Marquis EA, Seidman DN. Acta Mater 2005;53:4259–68.
[17] Drits MY, Ber LB, Bykov YG, Toropova LS, Anastaséva GK. Phys Met Metallogr 1984;57:118–26.
[18] Novotny GM, Ardell AJ. Mater Sci Eng A 2001;318:144–54.
[19] Iwamura S, Miura Y. Acta Mater 2004;52:591–600.
[20] Riddle YW, Saunders Jr TH. Metall Mater Trans A 2004;35:341–50.
[21] Watanabe C, Kondo T, Monzen R. Metall Mater Trans A 2004;35:3003–8.
[22] Watanabe C, Watanabe D, Monzen R. Mater Trans 2006;47:2285–91.
[23] Forbord B, Lefebvre W, Danoix F, Hallem H, Marthinsen K. Scripta Mater 2004;51:333–7.
[24] Fuller CB, Murray JL, Seidman DN. Acta Mater 2005;53:5401–13.
[25] Fuller CB, Seidman DN. Acta Mater 2005;53:5415–28.
[26] Tolley A, Radmilovic V, Dahmen U. Scripta Mater 2005;52:621–5.
[27] Clouet E, Lae L, Epicier T, Lefebvre W, Nastar M, Deschamps A. Nat Mater 2006;5:482–8.
[28] Deschamps A, Lae L, Guyot P. Acta Mater 2007;55:2775–83.
[29] Hallem H, Lefebvre W, Forbord B, Danoix F, Marthinsen K. Mater Sci Eng A 2006;421:154–60.
[30] Harada Y, Dunand D. Intermetallics 2009;17:17–24.
[31] High Tech Materials. Rare earths and specialty metals market prices; 2003.
[32] USGS. Mineral commodity summaries; 2007.
[33] Zalutskaya OI, Ryabov VR, Zalutsky II. Dopov Akad Nauk A 1969:255–9.
[34] Nie ZR, Jin TN, Fu JB, Xu GF, Yang JJ, Zhou J, et al. Mater Sci Forum 2002;396–402:1731–5.
[35] Nie ZR, Jin TN, Zou JX, Fu JB, Yang JJ, Zuo TY. Trans Nonferr Met Soc 2003;13:509–14.
[36] Yang JJ, Nie ZR, Jin TN, Xu GF, Fu JB, Ruan HQ, et al. Trans Nonferr Met Soc 2003;13:1035–9.
[37] Nie ZR, Fu JB, Zou JX, Jun TN, Yang JJ, Xu GF, et al. Mater Sci Forum 2004;28:197–201.
[38] Fu JB, Nie ZR, Jin TN, Zou JX, Zuo TY. J Rare Earth 2005;23:430–3.
[39] Mao JW, Jin TN, Xu GF, Nie ZR. Trans Nonferr Met Soc 2005;15:1341–5.
[40] Na H, Bian XF, Yin KB, Yao XJ. J Rare Earth 2005;23:474–7.
[41] Karnesky RA, van Dalen ME, Dunand DC, Seidman DN. Scripta Mater 2006;55:437–40.
[42] Knipling KE, Dunand DC, Seidman DN. Z Metallkd 2006;97:246–65.
[43] Xu GF, Mou SZ, Yang JJ, Jin TN, Nie ZR, Yin ZM. Trans Nonferr Met Soc 2006;16:598–603.
[44] van Dalen ME, Karnesky RA, Cabotaje J, Dunand DC, Seidman DN. Acta Mater; In press.
[45] Fujikawa SI. Defect Diffus Forum 1997;143:115–20.
[46] Murray JL. J Phase Equilib 1998;19:380–4.
[47] Hellman OC, Vandenbroucke JA, Rusing J, Isheim D, Seidman DN. Microsc Microanal 2000;6:437–44.
[48] Hellman OC, Vandenbroucke JA, du Rivage JB, Seidman DN. Mater Sci Eng A 2002;327:29–33.
[49] Ashby MF, Brown LM. Phil Mag 1963;8:1083–102.
[50] Ashby MF, Brown LM. Phil Mag 1963;8:1649–76.
[51] Karnesky RA, Sudbrack CK, Seidman DN. Scripta Mater 2007;57:353–6.
[52] Miller MK. Atom probe tomography: analysis at the atomic level. New York: Kluwer; 2000.
[53] Hyde JM, English CA. In: Lucas GE, Snead L, Kirk MA, Ellman RG, editors, Microstructural processes in irradiated materials, 2000. Materials research society symposia proceedings, vol. 650. Warrendale (PA): Materials Research Society; 2001. p. R.6.6.1–12.
[54] Umantsev A, Olson GB. Scripta Metall Mater 1993;29:1135–40.
[55] Kuehmann CJ, Voorhees PW. Metall Mater Trans A 1996;27:937–43.
[56] Nembach E. Particle strengthening of metals and alloys. New York: Wiley-Interscience; 1997.
[57] Karnesky RA, Martin G, Seidman DN. Scripta Mater; Submitted for publication.
[58] Zalutskaya OI, Kontsevoy VG, Karamyshev NI, Ryabov VR, Zalutsky II. Dopov Akad Nauk A 1970:751–3.
[59] Hyland Jr RW, Stiffler RC. Scripta Metall Mater 1991;25:473–7.
[60] Jo HH, Fujikawa SI. Mater Sci Eng A 1993;171:151–61.
[61] Asta M, Ozolins V, Woodward C. JOM 2001;53:16–9.
[62] Robson JD, Jones MJ, Prangnell PB. Acta Mater 2003;51:1453–68.
[63] Røyset J, Ryum N. Mater Sci Eng A 2005;396:409–22.
[64] Marquis EA, Riesterer JL, Seidman DN, Larson DJ. Microsc Microanal 2006;12:914–5.
[65] Mao Z. Personal communication; 2008.
[66] Baskes MI. Phys Rev B 1992;46:2727–42.
[67] Jian-Min Z, Fei M, Ke-Wei X. Chinese Phys 2004;13:1082–90.
[68] Balluffi RW, Allen SM, Carter WC. Kinetics of materials. Hoboken: Wiley-Interscience; 2005.
[69] Harada Y, Dunand DC. Mater Sci Eng A 2002;329–331:686–95.
[70] van Dalen ME. Ph.D. thesis, Northwestern University; 2007. URL: <http://nucapt.northwestern.edu/refbase/show.php?record=9848>.
[71] Mao Z, Sudbrack CK, Yoon KE, Martin G, Seidman DN. Nat Mater 2007;6:210–6.
[72] Clouet E, Barbu A, Lae L, Martin G. Acta Mater 2005;53:2313–25.
[73] Clouet E, Nastar M. Phys Rev B 2007;75:064109.